

Linear stability of flow in a 90-degree bend

Alexander Proskurin¹

*Altai state technical university 656038, Russian Federation, Barnaul, Lenin prospect,
46^{a)}*

The paper considers a two-dimensional flow in a channel, which consists of straight inlet and outlet branches and a circularly 90-degree curved bend. An incompressible viscous fluid flows through the elbow under the action of a constant pressure gradient between the inlet and outlet. Navier-Stokes equations were solved numerically using a high-fidelity spectral/hp element method. In a range of Reynolds numbers, an adaptive selective frequency dumping method was used to get a steady-state flow. It was found that three separation bubbles and vortex shedding can exist in the bend. The modal stability of two- and three-dimensional perturbations was investigated. Critical Reynolds number of the two-dimensional disturbances was found as extrapolation by lower Reynolds number results. It is much greater than three-dimensional one, but the two-dimensional flow could subcritically unstable with respect to the imposed small-amplitude white noise. For three-dimensional perturbations, the dependence of the critical Reynolds numbers on the bending radius is obtained. For a case of a moderate bending radius the neutral curve is provided and eigenfunctions are studied in detail: three-dimensional instability can be caused by periodic or monotonically growing mode, these unstable modes regard to the recirculation bubbles that occur after the bend.

I. INTRODUCTION

Complex shape channel flows, when there are recirculation bubbles, flow separation, and periodic motion, are often observed in nature and are widely used in industry. Depending on the Reynolds number, laminar, periodic, turbulent, and locally turbulent patterns can be realized. In the past 30 years, a generation of nonstationary regimes in such flows has been studied using the global stability theory. A review of such research is given in^{1,2}.

An example of flow with separation bubbles is the flow over a backward-facing step. The stability of this flow has been examined extensively and is discussed in several publications³⁻⁶. Kaikitis et al.⁵ investigated two-dimensional stability and found that the flow was globally-stable according to the linear analysis if $Re \leq 1000$. They show, that a large part of the flow domain is convectively unstable to the sustained upstream-generated finite-amplitude disturbances for Reynolds numbers $700 \leq Re \leq 2500$. Also, Kaikitis et al. assumed that the computations may perform global unsteadiness due to discretization errors that mask the convective instability of the flow.

Barkley et al.³ have presented the results of a study of the two- and three-dimensional linear stability of this flow. They found the critical Reynolds number for the three-dimensional perturbations ($Re_* = 748$) and have shown that the lower boundary of the critical Reynolds number for two-dimensional perturbations is much higher ($Re_{*2D} > 1500$). It proves the leading role of the three-dimensional perturbations. Barkley et al. also explain that the instability, according to the linear theory, is associated with the first recirculation bubble, which occurs immediately after the step, and the cen-

trifugal instability is responsible for generating secondary flow with the separation zone.

Lanzerstorfer et al.⁶ considered the backward-facing step flow stability for a systematic variation of the step height. It was found that the base flow lost its stability with respect to three-dimensional modes of different types, depending on the expansion ratio. Physical nature of instabilities is investigated by an energy transfer analysis. For very large step height, the instability has a centrifugal nature. In the case of moderate high step, an elliptical mechanism of perturbation growth is the most intense. For small-height steps, the base flow loses stability under the influence of lift-up mechanism. For large step height, the major mode is periodic, and when the height decreases, the instability begins to be determined by a monotonic mode.

Blackburn et al.⁴ examined optimal disturbances growth. They found that three-dimensional optimal disturbances had slightly larger growth in comparison to the two-dimensional. The three-dimensional mode appears near the step and gains energy downstream by the inviscid Orr mechanism and interaction of the Kelvin-Helmholtz instabilities of the two separated bubbles. Also, Blackburn et al. investigated the three-dimensional motion arising under the action of the random inflow noise. They observed a flow with a strong dominance of the two-dimensional dynamics.

Griffith et al.⁷ studied the flow in a partially blocked channel. On one side of the channel there was a semi-circular bump. The flow was investigated for range of the bump heights, the formation of the main recirculation bubble, minor bubbles, and vortex shedding at higher Reynolds numbers were found. The stability of this flow with respect to three-dimensional perturbations was studied. It was discovered that the critical Reynolds number decreases for higher blockage ratios and that the instability of this flow is determined by the elliptical mechanism rather than the centrifugal one.

Zhang&Pothérat⁸ investigated flow in a 180-degree

^{a)}Electronic mail: k210@list.ru

sharp bend. In the output branch of the bend, as the Reynolds number increases, the following patterns can exist: laminar, the appearance of the first recirculation bubble near the inner wall, and the appearance of the second recirculation bubble near the outer wall downstream of the first bubble. If the Reynolds number increases further, vortex shedding can occur in the outlet branch. It was also established that the flow patterns are similar to the flow near a circular cylinder, except for the symmetry, and that the two-dimensional dynamics determine the main features of the three-dimensional flow. Sapardi et al.⁹ studied the stability of this flow. It was shown that the flow can be unstable concerning to the three-dimensional periodic perturbations. Unstable modes are associated with the first recirculation bubble. A two-dimensional nonlinear stability analysis was also made and the hysteresis of the critical Reynolds numbers was found.

Heskestad¹⁰ studied the air flow in a sharply curved channel experimentally and compared the results with the predictions free-streamlines theory. Yamashita et al.¹¹ investigated the flow of water and air in a two-dimensional sharp 90-degree bend. They obtained data on the pressure drop and the distribution of the average velocity, velocity fluctuations, the streamlines and the energy spectrum of velocity fluctuations, detected laminar and turbulent types of the flow, observed experimentally a vortex shedding in the range $Re = 172.5 - 750$ (Reynolds number converted to this article parameters) where the first number was the lower boundary for the unsteady motion.

Matsumoto et al.¹² studied systematically two-dimensional flow patterns in a sharply bent channel for angles less than 90 degrees and describe recirculation bubbles in the outer angle of the bend and near the inner wall of the outlet branch right after the bend. They also observed the periodic vortex emission in the outlet branch and have described conditions for each pattern. Matsumoto et al.¹² especially notes that the intermediate regimes between the turbulent and the laminar in the bend even are poorly studied.

Hurd&Peters¹³, Orlandi&Gunsolo¹⁴ studied numerically the laminar flow in a smoothly curved channel and Hurd&Peters¹³ compared the calculated velocity profiles with their experimental results. Kotb et al.¹⁵ presented results of a numerical study of the flow in a curved channel were taking attention to the size of the separation regions dependence on the Reynolds number and the bending radius.

Donghun&Seung Park¹⁶ studied nonlinear stability of the smooth bent flow in the case of small bent angles which were less than 60 degrees and a large bending radius. For such small curvature stability modes shape close to the case of the straight Poiseuille flow. They describe the nonlinear interaction of the oblique waves, and the amplification of streamwise streaks and vortices. The amplitude of the streaks increases in the bend and the outlet branch, but the streamwise vortices increases

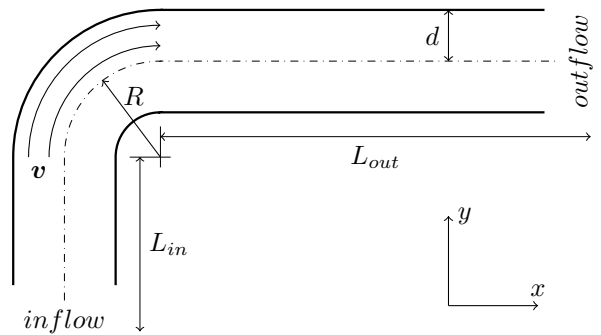


FIG. 1. The bent channel

only in the bend.

Niu&Dou¹⁷, Lupi et al.¹⁸ studied the stability of the flow in 90-degree pipe bends. Niu&Dou considered the square cross-section duct using energy gradient theory. Lupi et al.¹⁸ investigated a bend of circular pipe and they found using direct numerical modeling that the flow was stable for $Re < 2500$. A pair of counter-rotating Dean vortices was observed. The presence of two recirculation regions is detected inside the bend: one on the outer wall and the other on the inner side right after the bend. At $Re > 2500$, a periodically oscillating flow was caused by a linear mode, which becomes growing at $Re = 2531$. Lupi et al. concluded that the disturbances increase inside the outer recirculation bubble due to a large shear in the backflow.

The problem is defined in section II. The numerical method presentation and calculations set up are described in section III. Sections IV, V outline possible flow regimes and sections VI, VII describes results of the investigations of two- and three-dimensional stability. The conclusion VIII summarizes the main findings.

II. PROBLEM FORMULATION

Figure 1 shows a bent flow. The channel consists of two parallel impermeable surfaces. The length of the straight inlet and outlet sections is equal L_{in} and L_{out} respectively. The bending radius on the centre line is equal to R . The distance between the surfaces is constant and is equal to $2d$. A bending parameter is $\delta = R/2d$. The paper considers the case of $\delta = 1$, $L_{in} = 10$ and $L_{out} = 60$. The incompressible viscous fluid flows under the action of a constant pressure difference between the inflow and the outflow. The Reynolds number $Re = \frac{Ud}{\nu}$ was introduced, where U is the maximum velocity of the laminar Poiseuille flow, and ν is the fluid viscosity. The Navier-Stokes equation is

$$\frac{\partial \mathbf{V}}{\partial t} + (\mathbf{V} \cdot \nabla) \mathbf{V} = -\nabla p + \frac{1}{Re} \Delta \mathbf{V} + \mathbf{F}, \quad (1)$$

$$\nabla \cdot \mathbf{V} = 0,$$

where \mathbf{V} is the velocity, \mathbf{F} is the external force, and p is the pressure. At the channel walls, the no-slip condition $\mathbf{V} = 0$ holds true. The Poiseuille parabolic profile $V_y = 1 - x^2$ is imposed at the inflow. At the outflow, the standard boundary conditions is imposed^{3,6,7,9}

$$\frac{\partial V}{\partial x} = 0, \quad p = 0. \quad (2)$$

On all other boundaries the pressure satisfies the high-order Neumann condition¹⁹.

If $\mathbf{U}(x, y)$ is a steady-state solution of (1), this equation can take a linearized form

$$\frac{\partial \mathbf{v}}{\partial t} + (\mathbf{U} \cdot \nabla) \mathbf{v} + (\mathbf{v} \cdot \nabla) \mathbf{U} = -\nabla p + \frac{1}{Re} \Delta \mathbf{v}, \quad (3)$$

$$\nabla \cdot \mathbf{V} = 0,$$

where $\mathbf{v}(x, y, z, t)$ and $p(x, y, z, t)$ are the small disturbances. Since the baseflow $\mathbf{U}(x, y)$ is two-dimensional, the disturbances may be written as

$$\begin{aligned} \mathbf{v}(x, y, z, t) &= \mathbf{v}(x, y) e^{(\sigma + i\omega)t + i\beta z} + \text{c.c.}, \\ p(x, y, z, t) &= p(x, y) e^{(\sigma + i\omega)t + i\beta z} + \text{c.c.}, \end{aligned} \quad (4)$$

where σ is the disturbance growth-rate, ω is the disturbance frequency, and the spanwise wave number is $\beta = \frac{2\pi}{\lambda}$, where λ is the spanwise wavelength. The substitution (4) allows to decouple the three-dimensional stability problem (3) to a series of two-dimensional problems for each value of β , which varies continuously. This analytical transformation was used by^{1,3,9} and many others.

Boundary conditions for the disturbance have the form

$$\begin{aligned} \mathbf{v} &= 0 \text{ at the walls and the inflow,} \\ \frac{\partial \mathbf{v}}{\partial x} &= 0, \quad p = 0 \text{ at the outflow} \end{aligned} \quad (5)$$

III. METHODOLOGY, NUMERICAL METHOD AND CONVERGENCE

The baseflow and stability calculations were made by the open source spectral/hp element framework Nektar++²⁰. The multi-element formulation gives geometric flexibility by comparison to the single-domain spectral methods, and allows to implement the high-order approach to complex shape flows. High-order methods can improve the reliability, accuracy, and computational efficiency of calculations.

To integrate the equations (1), Nektar++ uses the well-known splitting scheme that decouples the velocity and the pressure¹⁹. From equations (3) a linear operator \mathbf{A} can be constructed:

$$\mathbf{v}(x, y, z, \tau) = \mathbf{A}(\tau) \mathbf{v}(x, y, z, 0) = \lambda(\tau) \mathbf{v}(x, y, z, 0), \quad (6)$$

where τ is a time interval. $\mathbf{A}(\tau)$ is constructed numerically by the splitting procedure in the same way as in the

case of nonlinear equations. In order to find an eigenvalue $\lambda(\tau)$, it is convenient to construct a Krylov subspace

$$K_n(\mathbf{A}, \mathbf{v}_0) = \text{span}\{\mathbf{v}_0, \mathbf{A}(T)\mathbf{v}_0, \mathbf{A}(T)^2\mathbf{v}_0, \dots, \mathbf{A}(T)^{n-1}\mathbf{v}_0\}, \quad (7)$$

where $\mathbf{A}(\tau)^i \mathbf{v}_0$ is obtained by direct calculation $\mathbf{v}_1 = \mathbf{A}(\tau)\mathbf{v}_0$, $\mathbf{v}_2 = \mathbf{A}(\tau)\mathbf{v}_1$, Further eigenvalue calculations are carried out by standard numerical algebraic techniques, such as the Arnoldi method. The eigenvalues are obtained by Nektar++ in the form:

$$\lambda(\tau) = m \cdot e^{\theta i}, \quad (8)$$

and if $m > 1$ then the flow is unstable. The time-independent growth is $\sigma = \frac{\ln(m)}{\tau}$ and the time-independent frequency is $\omega = \frac{\theta}{\tau}$.

For eigenvalue problem it is possible to use a direct coupled approach developed by Sherwin&Ainsworth²¹ and also implemented in Nektar++. A weak form of the Stokes problem can be considered

$$\begin{aligned} \left(\nabla \phi, \frac{1}{Re} \nabla \mathbf{v} \right) - (\nabla \cdot \phi, p) &= (\phi, \mathbf{f}), \\ (q, \nabla \cdot \mathbf{v}) &= 0, \end{aligned} \quad (9)$$

where $\mathbf{v}, \phi \in \mathbf{V}$, $p, q \in W$ and \mathbf{v} , W are appropriate spaces for the velocity and pressure system to satisfy inf-sup condition. To complete system (9) to the Navier-Stokes problem, the advection terms $(\mathbf{U} \cdot \nabla) \mathbf{v} + (\mathbf{v} \cdot \nabla) \mathbf{U}$ are included as force \mathbf{f} . Next, the Arnoldi method is applied.

Figure 2 shows the mesh that was used for the calculations. This mesh contains 685 elements and is employed for flow at Reynolds number $Re = 500 \sim 800$. For higher Reynolds numbers, meshes with more elements were used; for smaller Re , less detailed meshes are optimal.

The steady-state flow was found by integrating equations (1) in time until a constant velocity was observed at the selected points and the time convergence was achieved in at least 9 – 10 digits. Some of these points are marked with crosses in figure 3, the numbers increase from left (No 1) to right (No 4). Table I shows the values of the horizontal velocity and the growth depending on the order of the approximation polynomials p . Velocity converges up to 6 digits or 0.0001% of the velocity scale U . Table I also shows the σ convergence for the leading (real) mode at $\beta = 1.0$. The table also include σ convergence for base flow time T . Most of the results below were obtained at $T = 500 - 1000$ and the approximation order is $p_s = 7$ for the base flow and $p_s = 10 - 12$ for the eigenvalues.

The eigenvalues and the base flow may depend on the length of the inlet and outlet branches of the channel. For verification, a series of calculations was performed with different L_{in} and L_{out} at $Re = 710$, close to the critical Reynolds number. The results of these calculations are shown in the table II. It was found that in the range $10 \leq L_{in} \leq 40$ and $40 \leq L_{out} \leq 120$ hold $\sigma_{max} - \sigma_{min} =$

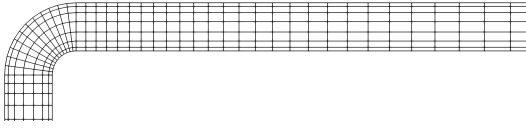


FIG. 2. Part of the mesh near the bend

$2.5 \cdot 10^{-6}$ This means that the effect the inlet and outlet lengths to the eigenvalues for $L_{in} \geq 10$ and $L_{out} \geq 40$ is less than the calculations error. Such check was performed not only for $Re = 710$, but also for larger Reynolds numbers.

Åkervik et al.²² describe a selective frequency damping method that can converge to an unstable flow. This is a replacement of the Newton method, and it is easier to use since the method does not require a high quality initial condition. However, the selective frequency damping method requires a very large computational cost.

Jordy et al. in their article²³ describe an adaptive selective frequency dumping method, which applies one-dimensional reduced model to find these parameters. The adaptive selective frequency damping method is implemented in the Nektar++ framework^{23,24}. The complete numerical calculations set up and the convergence analysis are presented in article²⁵.

A nonlinear form of the advection terms

$$(\mathbf{V} \cdot \nabla) \mathbf{V} = (\mathbf{U} \cdot \nabla) \mathbf{v} + (\mathbf{v} \cdot \nabla) \mathbf{U} + (\mathbf{v} \cdot \nabla) \mathbf{v} \quad (10)$$

can be used to split the base flow and the disturbance dynamics calculations. Appropriate modification of the Nektar++ code was reported in^{26,27}. This approach allows the study of the nonlinear disturbances near the stabilized base flow.

IV. FLOW REGIMES

Figure 4 shows streamlines at $\delta = 1$ and $Re = 20, 200, 500, 1300$. The flow is laminar at small Reynolds numbers and its streamlines are parallel (see 4(a)). When the Reynolds number increases, vortices $V1, V3$ and $V2$ (see 4(b,c,d)) appear. For relatively high Reynolds numbers it is possible for two different flow patterns to exist: the steady-state and the pulsating. The pulsating pattern is shown in figure 4(e). One of the two patterns can exist depending on the conditions that are described later in the article.

Figure 5 presents a vortex diagram in the bend. $V3$ vortex area is marked by circles, $V1$ by squares, and $V2$ by diamonds. To calculate the end position of the vortices, a curved coordinate system is introduced, the axis where x_a is aligned along the axis of the channel. The ends of the vortices are projected onto it, as shown on top panel in figure 5 using dotted lines.

Matsumoto et al.¹² found the vortices $V1, V2$ in the sharp bend. Zhang&Pothérat and Sapardi et al.^{8,9} found vortices $V1, V2$, and $V3$ in the 180-degree sharp bend, where $V1$ vortex has a great influence on the flow's characteristics. Articles^{8,9,12} also describe the appearance of the pulsating flow.

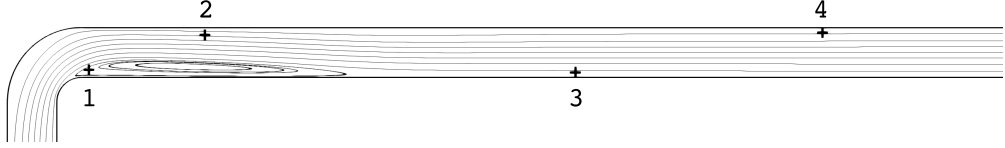
V. THE PULSATILE FLOW

This section presents the results of a study of the pulsations that are observed in the outlet branch at moderate Reynolds numbers. Matsumoto et al.¹² have found such non-stationary patterns in the sharp bend. Zang&Pothérat and Sapardi et al.^{8,9} found such vortex shedding in the sharp 180-degree bend. Sapardi et al. have found the large hysteresis for the critical Reynolds number that depends from the initial conditions. They found for a special case, that $Re'_* \approx 1150$ for calculations from rest, or the lower Reynolds number steady-state velocity field, and $Re'_* = 743$ for calculations from the unsteady initial condition. The apostrophe here means that they calculated the critical Reynolds number by the channel width and $Re = 0.5Re'$. Yamasita et al.¹¹ experimentally observed the pulsatile flow in a sharp two-dimensional bend at $Re > 172.5 - 750$ (Reynolds number converted to this article parameters).

During routine calculations for this investigation, it had observed that an increase in the quality of the approximation, i.e., a decrease in the time step, an increase in the order of approximation p , or the number of mesh elements, suppresses the vortex shedding. Therefore, it is possible to assume that these pulsations arise due to the instability of the flow under the influence of perturbations imposed by the numerical scheme noise.

To prove this hypothesis, the perturbation was imposed as the force \mathbf{F} (see (1)) of the random amplitude A for the two-dimensional base flow. The values of this force were updated at each time step. Figure 6(a) shows the flow response as the dependencies of the maximum vertical velocity amplitude on the centre line of the outlet branch from the noise amplitude. The curve $\mathbf{U} = 0$ shows the response in the case of the rest fluid, when there is no gain due to the instability. In the case of $Re = 200$ this response is smaller than for the rest fluid and the perturbations do not grow because disturbance flow out from the channel. In the cases $Re = 500$ and $Re = 800$ the perturbations are amplified, and when $Re = 800$, the motion amplitude is 10^2 times greater compared to the rest fluid.

Figure 6(b) shows graphs of the kinetic energy of the perturbation under the noise with the amplitude $A = 10^{-3}$. At $Re = 10$, the perturbation energy is slightly lower than at $Re = 500$, and for these cases the energy of the forced motion remains relatively small. At $Re = 800$, the energy of the perturbed motion at the initial step has the same level as at $Re = 500$. At $t \approx 50$ this energy increases at least 10 times and the oscilla-

FIG. 3. The control points, $Re = 600$ TABLE I. The convergence of the growth σ and the horizontal velocity v_x at the control points, $Re = 600$. Calculations were made on the mesh containing 685 elements exclude a column for which the mesh size was 1341 element. p_b was the order of approximation for the base flow, p_s was the same for the stability calculations. Alone p means $p_b = p_s$. The tolerance was 10^{-8}

p	Point 1	Point 2	Point 3	Point 4	σ	σ , 1341 elem.	T	$p_b = 7, p_s = 7$	$p_b = 7, p_s = 10$
5	-0.0097407	1.046623711	0.27554782	0.32007041	-0.00362109	-0.00341311	100	-0.00349753	-0.00350349
7	-0.0085206	1.046248285	0.27560974	0.32013706	-0.00378192	-0.00378138	250	-0.00377620	-0.00378212
10	-0.0084460	1.046219465	0.27561238	0.32013999	-0.00378744	-0.00378506	500	-0.00378192	-0.00378723
12	-0.0084454	1.046219463	0.27561233	0.32013996	-0.00378747	-0.00378506	1000	-0.00378192	-0.00378724

tory motion continues at this energy level. If the noise was been switched off at time $t = 200$, the pulsating motion faded. Thus, the pulsations must be supported by permanent external impulsion.

Figure 7 presents the vertical velocity on the outlet branch centre line at several consecutive moments in time after the noise is turned on. Each period of the graph corresponds to one vortex. Vortices are arising near the trailing edge of V2. The velocity amplitude of each vortex increases downstream and reaches a maximum at $x > 50$. Then each vortex moves with its own amplitude until it leaves the channel. The amplitude of the vortices along the longitudinal coordinate x fluctuates in some way, not quite exactly periodically. This means that the vortex path is modulated in amplitude in the longitudinal direction, in other words, a sequence of vortex packets forms in the channel.

It is known that some flows can amplify disturbances. Boujo&Gallaire²⁸ studied this phenomenon in the flow over the backward-facing step and found that the steady-state flow is stable, but disturbances can increase in space and time as a result of non-normal effects. As is clear from the above results, this amplification are observed in the bent flow. In context of this investigation, this phenomenon is completely eliminated by increasing the accuracy of calculations or using the selective frequency dumping method.

VI. STABILITY OF THE TWO-DIMENSIONAL FLOW

This section considers the stability of the two-dimensional perturbations at $\delta = 1$. The base steady-state flow was calculated up to $Re \sim 1200$ by time-integrating the equations (1). For larger Reynolds numbers, the adaptive selective frequency dumping method described above was applied. With this method, it was possible to calculate the steady-state flow up to $Re = 1900$. The direct solver was used for eigenvalues

together with the SFD baseflow calculations, because in this case the time-dependent scheme (6) is unstable for the same reason as for the baseflow.

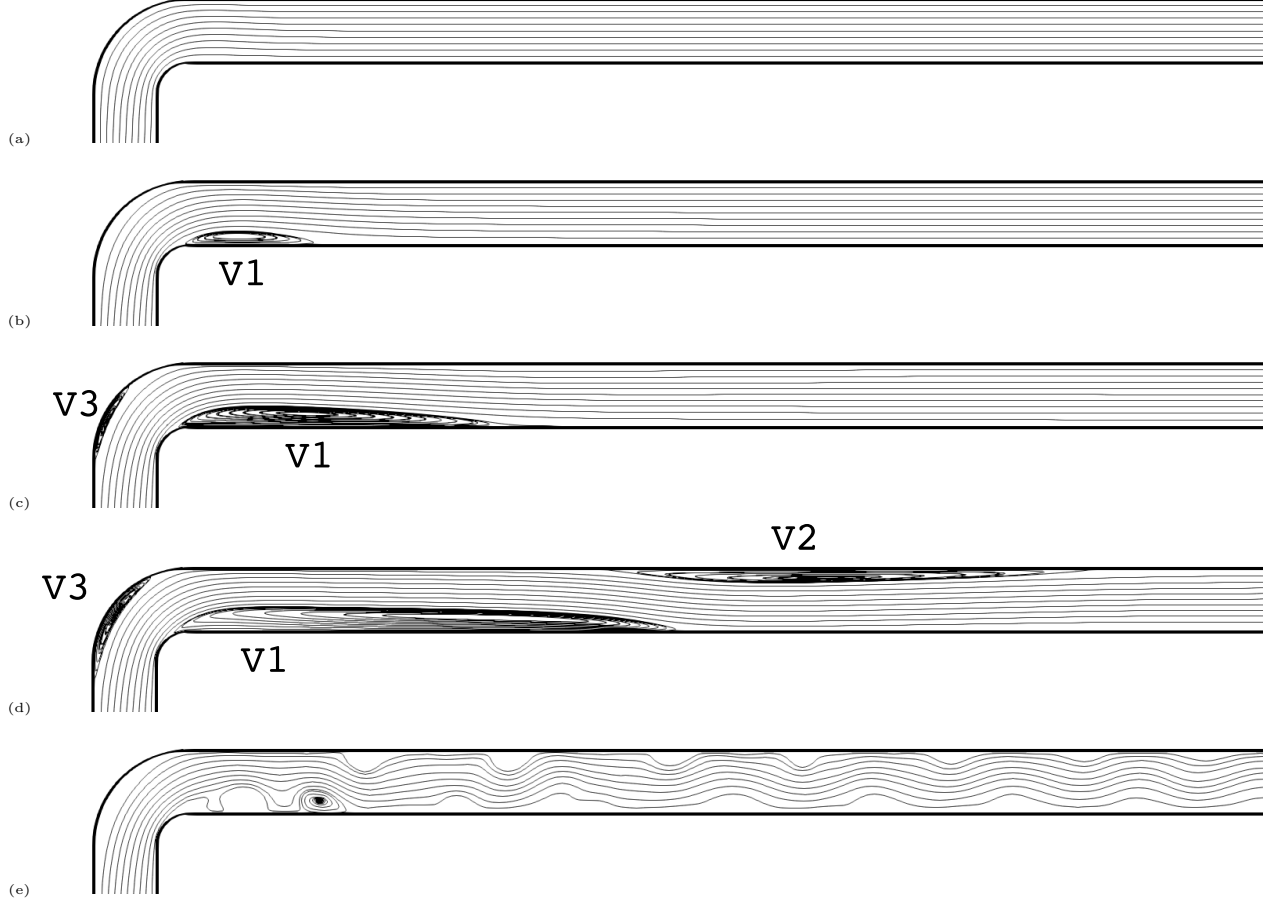
In Figure 8 presents the eigenvalues for $Re = 1800$ and $\delta = 1.0$. The most dangerous is the monotonic mode. Figure 9 shows the dependencies of σ from Re . In this graph, all σ values are lower than zero, so the two-dimensional perturbations are stable up to $Re = 1900$. A dashed line represents an approximation $\sigma(Re)$ for $900 \leq Re \leq 1900$ using the least squares method. The appropriate critical Reynolds number is $Re_* = 3495$. Figure 10 shows the streamlines of the base flow(a) and the leading mode(b) at $Re = 1600$, and the vertical velocity amplitude(c). Thus, the most dangerous mode is localized at downstream the recirculation bubble V2.

VII. LINEAR STABILITY

This section summarizes the results of studying three-dimensional linear stability in the bent channel. Figure 11 presents the growth σ (a) and frequency ω (b) at $Re = 1400$ as function of the spanwise wavenumber $\beta = \frac{2\pi}{L}$. Solid markers signify real modes, and hollow markers – complex modes. The graph 11 is plotted in the range $0.01 < \beta < 10$, outside of which the flow is stable. Small values of β correspond to perturbations with a very large spanwise wavelength, and, in limit case $\beta \rightarrow 0$, fit to the two-dimensional case. In the case of large β spanwise wavelength of the perturbation is short. The leading real mode is indicated by solid rectangles. It has a maximum at $\beta \approx 2.2$. In the range of $0.11 < \beta < 0.44$, the leading mode is complex. For sufficiently large Reynolds numbers, this mode can be unstable. The spatial structure of unstable modes will be considered below. Solid diamonds denote a real mode that is the leading at $\beta < 0.11$, and this mode is stable. Empty circles and diamonds mark complex modes. Their amplitude sufficiently large in the downstream area. Also, the graph shows several minor

TABLE II. The influence of L_{in} and L_{out} on the growth σ at $Re = 710$

L_{in}	L_{out}	σ	L_{in}	L_{out}	σ	L_{in}	L_{out}	σ
5	60	-0.00005779	10	40	0.00012109	10	60	0.00012108
10	60	0.00012108	10	60	0.00012108	20	80	0.00012352
20	60	0.00012351	10	80	0.00012111	30	100	0.00012353
30	60	0.00012351	10	100	0.00012109	40	120	0.00012116

FIG. 4. The base flow patterns: $Re = 20$ (a), $Re = 200$ (b), $Re = 500$ (c), $Re = 1300$ (d)(the steady-state flow), $Re = 1300$ (e)(the pulsating flow)

stable modes.

Figure 12 shows the dependencies of the growth σ on the spanwise wavenumber β at $Re = 300, 700, 1100, 1900$. Each curve is made up of the values of σ that correspond to the major mode. The real eigenvalues in this figure are marked by solid symbols, and the complex ones by hollow symbols. At $Re = 300$, the curve has local maxima at $\beta \approx 0.03$ and $\beta \approx 1.0$, the first of which corresponds to the complex mode, and the second to the real mode. When β decreases, the frequency also decreases. As the Reynolds number rises, the real mode first becomes unstable and there is a finite range of the spanwise wavenumbers for unstable modes. With a further increase in the Reynolds number, the left boundary

of this interval is determined by periodical perturbations. Periodic modes also dominate at large β , but they are stable.

A neutral curve is presented in Figure 13. This figure shows a area of instability for $Re < 1900$. The border points on the curve were obtained by detecting the zero-growth point by varying β at a fixed Reynolds number. The unstable modes exist in the shaded area. The smallest value of the Reynolds number Re_* , which is associated with the critical wave number β_* . Empty diamonds indicate the boundary where the leading modes change from the real mode to the complex mode. Empty triangles denote the neutral boundary for the complex

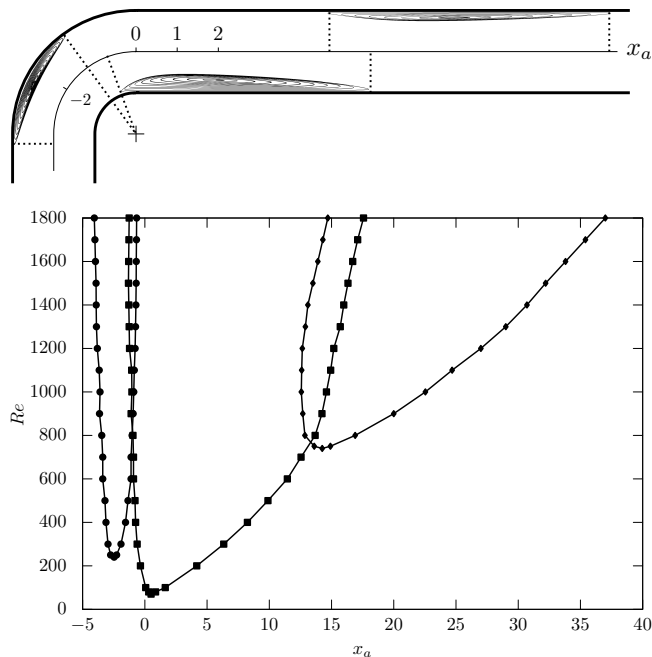


FIG. 5. Flow diagram, $\delta = 1$, the circles indicate the appearance of V3 recirculation bubble, rectangles – V1, diamonds – V2, the dashed line is rough lower border for the pulsating flow origin. The top panel shows a curvilinear coordinates with an axle x_a and projections of the separation points on the axle

mode.

For the Reynolds number 1100, the leading unstable mode is real and is concentrated near the first recirculation bubble, as shown in Figure 14 using isosurfaces of the longitudinal vorticity component (a) and the transverse velocity component in the place of maximal amplitude (aa). The spectra for this parameters' values are presented in Figure 15(a). Since the mode is localized in the area of the first separation bubble, it can be called a bubble mode (*B*-mode). When the transverse wavenumber β decreases, the leading unstable eigenfunction has a noticeable, albeit smaller, amplitude in the region of the second recirculation bubble, as shown in Figure 14 (b, bb). In this case, the corresponding eigenvalue remains real. This mode couple first and second recirculation bubbles and can be named *C*-mode. In Figure 13 the stability boundary of the *B*-mode is indicated by solid circles, and the stability boundary of the real *C*-mode is indicated by solid diamonds.

As the Reynolds number increases, there is a complex *C*-mode, the real and imaginary parts of which are shown in the figures 14 (c, cc, d, dd) for $Re = 1600$, $\beta = 0.3$. As can be seen from the figure 15 (b), there is only a pair of complex eigenvalues above the line $\sigma = 0$, while the real modes are stable. In contrast to long transverse perturbations (small β), short-wave perturbations are concentrated near the tail of the first recirculation

TABLE III. The critical Reynolds numbers Re_* and the corresponding spanwise wavenumbers β_*

δ	0.7	1.0	1.5	2.0	2.5
$Re_*, \pm 1$	469	705	1187	1852	2737
$\beta_*, \pm 0.01$	1.01	0.99	0.96	0.89	0.79

bubble, as shown in Figure 14 (e, ee) at $Re = 1600$, $\beta = 3.0$. The corresponding spectra are shown in Figure 15 (c). The eigenvalue of the leading mode is real. This fashion can be called a tail fashion (*T*-mode). The stability boundary of the *T*-mode is shown by solid rectangles in the figure 13. It should be noted that a clear threshold exists only when the real *B*-mode changes the complex *C*-mode. The transition between the real *B*, *C* and *T* modes when the Re or β change is carried out by progressive increase of the velocity amplitude in one bubble and decrease in the other.

Figure 16 shows selected minor eigenfunctions at $Re = 1400$: $\beta = 1.0$ (a), $\beta = 0.4$ (b, real part). In the figure 11 these modes are indicated by filled rectangles and empty circles, respectively. From figure 11 ones can see that several periodic modes have forks. As example, the leading periodic *C*-mode (empty rectangles in Figure 11) at $\beta \approx 0.44$ branches into two real ones (filled rectangles in the same figure), upper and lower. There is a real *C*-mode exists near the branching point. With a further increase in β , the upper branch corresponds to instability inside the recirculation bubble V1, and the lower branch corresponds to V2. The patterns shown in figure 16 (b) correspond to the oblique modes that are observed in the plane channel. It can significantly affect the stability with the small curvature channel¹⁶.

The dependences of the critical Reynolds numbers on the bending radius are given in table III. The critical Reynolds number increases almost ten times by increasing the bending parameter, and when $\delta = 2.5$ it has the same order of magnitude as for the plane flow. The corresponding critical modes are real.

VIII. CONCLUSIONS

Two-dimensional flow regimes in a curved channel have been investigated. It was found that as the Reynolds number increases, three recirculation bubbles appear sequentially. At relatively large Reynolds number, a regime with non-stationary vortex shedding may occur. Such vortex generation was observed earlier in a channel with a back-face step, and in a sharp bend (numerically and experimentally). The vortex shedding is being sustained due to the existence of approximation errors that produce persistent noise. The lower limit of the pulsations impossible to determine exactly. By reducing the calculation error the steady-state flow was found up to $Re \approx 1200$

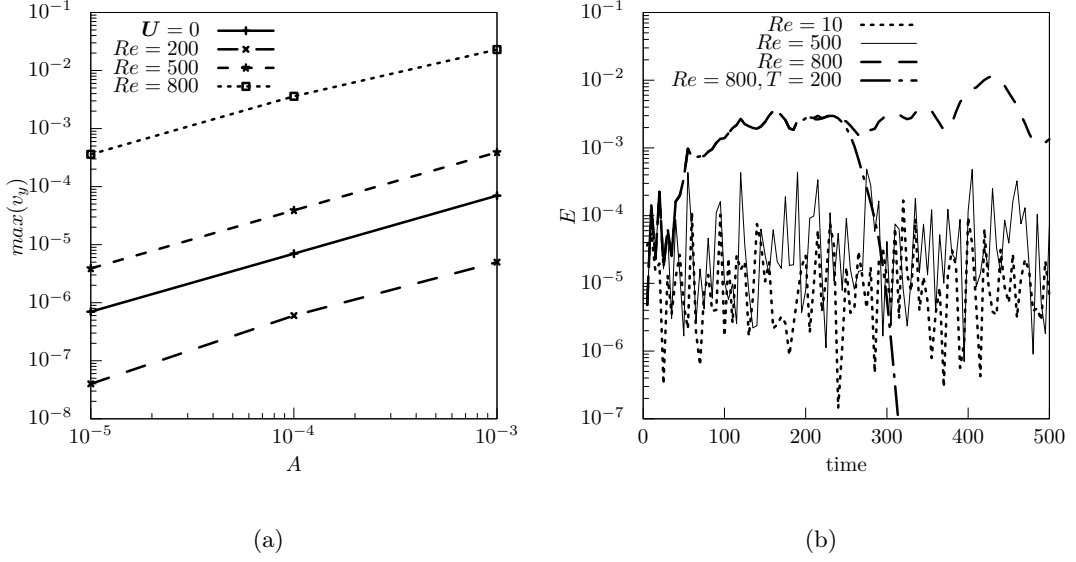


FIG. 6. The response for the random noise as the vertical velocity v_y maximal amplitude in the outlet branch centre line for the motionless fluid and $Re = 200, 500, 800$ (a); The disturbance energy for $Re = 10, 500, 800$ for the permanent noise amplitude $A = 10^{-3}$ and, for the case $Re = 800$, the noise had been switched off at $t = 200$ (b)

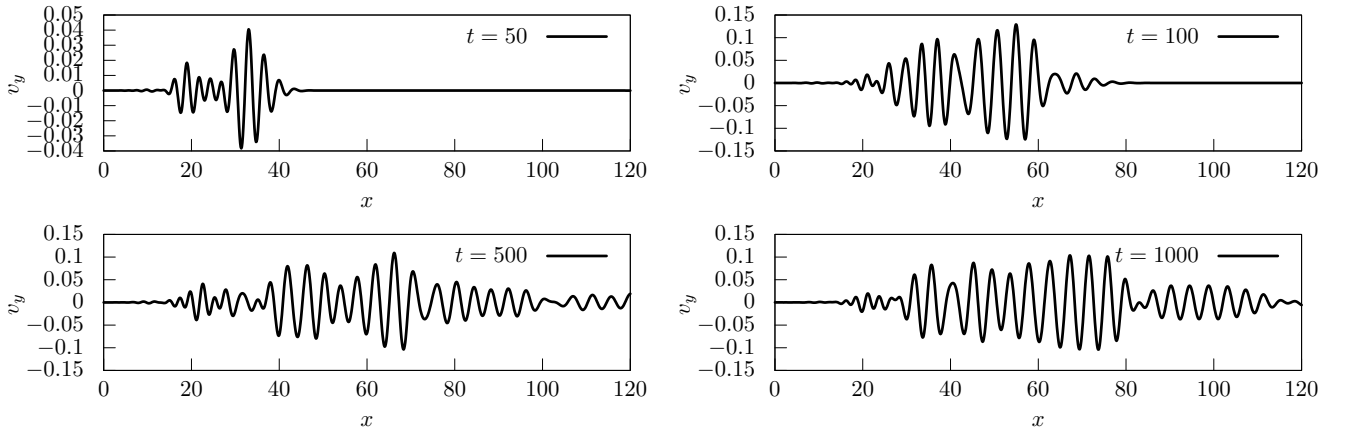


FIG. 7. The graphs of the vertical velocity v_y at the outlet branch centreline for $t = 50, 100, 500, 1000$, $Re = 1000$

in the present calculations. At $1200 < Re < 1900$, the steady-state solution was obtained using the selective frequency dumping method.

The flow is linearly stable according to the two-dimensional perturbations at $Re < 1900$, which allows to exclude the exponential growth of an unstable mode as a possible mechanism for the pulsations. It was found above that the bent flow can amplify the noise of very small amplitude $\sim 10^{-5}$. This is likely that disturbances grow up under influence of non-orthogonality effects. This scenario is supported by the results of^{4,28}. On the other hand, the amplitude of the resulting disturbance is large enough for noticeable influence of the nonlinear interaction mechanisms. Taking into account

these considerations, it is possible to assume the existence of a two-stage scenario of subcritical transition to the pulsatile flow.

There is a range of spanwise wave numbers β where leading three-dimensional modes grow. These modes can be periodic when the corresponding eigenvalue is complex or monotonic for real eigenvalues. The periodic mode has significant amplitude inside the first and second separation bubbles. It is the leading mode for smaller β in the range of instability. If the spanwise wave-number β increases, the periodic mode splits into two monotonic modes, which correspond to the first and second recirculation bubbles. The amplitude of the leading real unstable mode concentrates in the first recirculation bub-

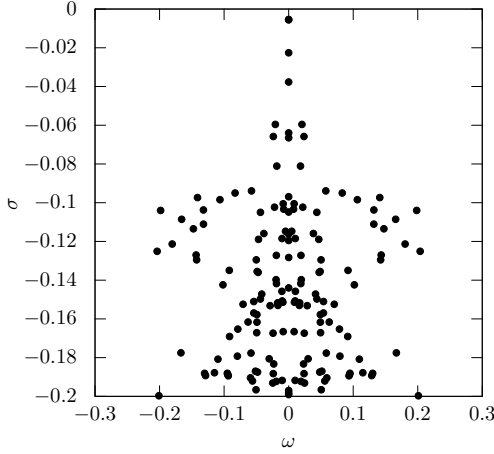


FIG. 8. The eigenvalues at $Re = 1800$, $\delta = 1$

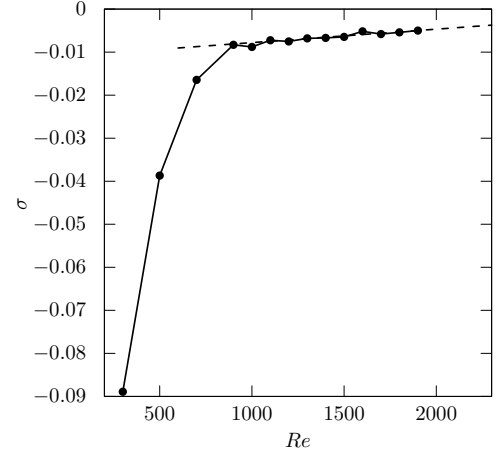


FIG. 9. The growth σ form Re for the 2D disturbances, the dashed line is the least squares approximation for $Re > 900$

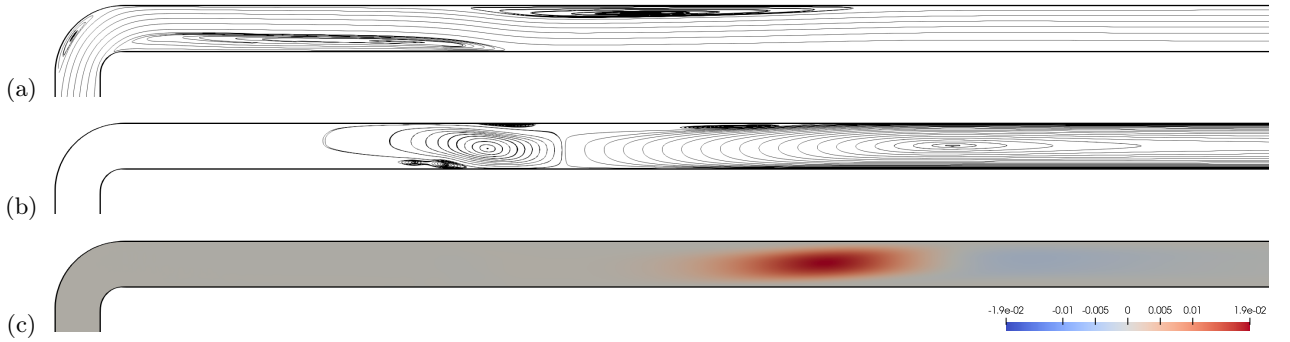


FIG. 10. The stabilized flow streamlines at $Re = 1600$ (a), its leading eigenfunction (b) and the vertical velocity amplitude (c)

ble. Based on the results of^{3,6,7,18}, we can list possible mechanisms of instability occurrence in the bent channel: centrifugal^{3,6,7}, elliptical^{6,7}, lift-up⁶, shear instability of the backflow¹⁸. Since the flow is complex in space, they can act simultaneously and it is difficult to detect one of them. with high degree of certainty the lift-up mechanism can be excluded, since unstable eigenfunction does not contain alternating slow and fast streaks. In the case of the dominance of shear instability, one would expect a large amplitude of the eigenfunction in the region of the largest gradient of the reverse flow, which is not confirmed by the results. Therefore, the main possible mechanisms of instability at $\delta = 1$ can be identified as elliptical and centrifugal.

IX. DATA AVAILABILITY

The data that support the findings of this study are available from the corresponding author upon reasonable

request.

X. *

The manuscript is under consideration in Physics of Fluids.

¹V. Theofilis. Global linear instability. *Annual Review of Fluid Mechanics*, 43:319–352, 2011.

²Kunihiko Taira, Maziar S Hemati, Steven L Brunton, Yiyang Sun, Karthik Duraisamy, Shervin Bagheri, Scott TM Dawson, and Chi-An Yeh. Modal analysis of fluid flows: Applications and outlook. *AIAA journal*, 58(3):998–1022, 2020.

³Dwight Barkley, M Gabriela M Gomes, and Ronald D Henderson. Three-dimensional instability in flow over a backward-facing step. *Journal of Fluid Mechanics*, 473:167–190, 2002.

⁴Hugh Maurice Blackburn, Dwight Barkley, and Spencer J Sherwin. Convective instability and transient growth in flow over a backward-facing step. *Journal of Fluid Mechanics*, 603:271, 2008.

⁵Lambros Kaiktsis, George Em Karniadakis, and Steven A Orszag. Unsteadiness and convective instabilities in two-

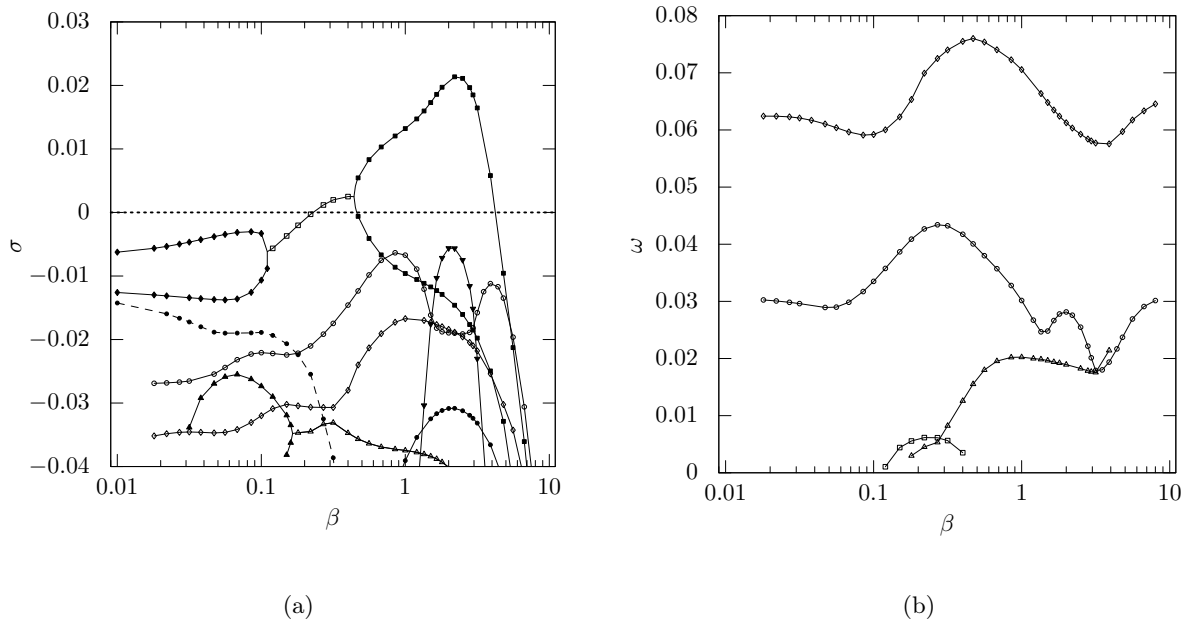


FIG. 11. The eigenvalues at $Re = 1400$ as function of spanwise wavenumber β : growth σ (a) and frequency ω (b). Only positive frequencies are shown here.

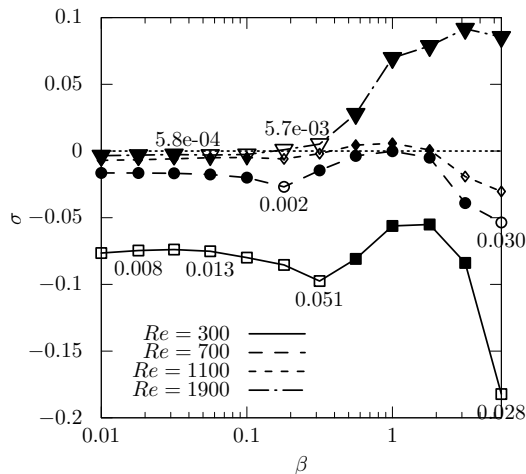


FIG. 12. Leading growths σ at $Re = 300, 700, 1100, 1900$ as function of the spanwise wavenumber β . Solid points represent real eigenvalues, hollow points represent complex eigenvalues. Numbers near selected points show value of the frequency ω . Lines connect leading eigenvalues for each Reynolds number.

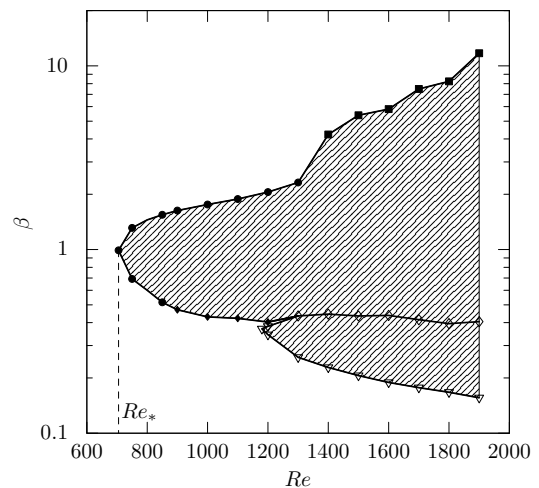


FIG. 13. Neutral stability curve for the bent flow. Filled region includes parameters' values for which the flow is unstable.

dimensional flow over a backward-facing step. *Journal of Fluid Mechanics*, 321:157–187, 1996.

⁶Daniel Lanzerstorfer and Hendrik C Kuhlmann. Global stability of the two-dimensional flow over a backward-facing step. *Journal of fluid mechanics*, 693:1, 2012.

⁷Martin D Griffith, Mark C Thompson, Thomas Lewke, Kerry Hourigan, and Warwick P Anderson. Wake behaviour and in-

stability of flow through a partially blocked channel. *Journal of Fluid Mechanics*, 582:319–340, 2007.

⁸Lintao Zhang and Alban Poth  rat. Influence of the geometry on the two-and three-dimensional dynamics of the flow in a 180 sharp bend. *Physics of Fluids*, 25(5):053605, 2013.

⁹Azan M Sapardi, Wisam K Hussam, Alban Poth  rat, and Gregory J Sheard. Linear stability of confined flow around a 180-

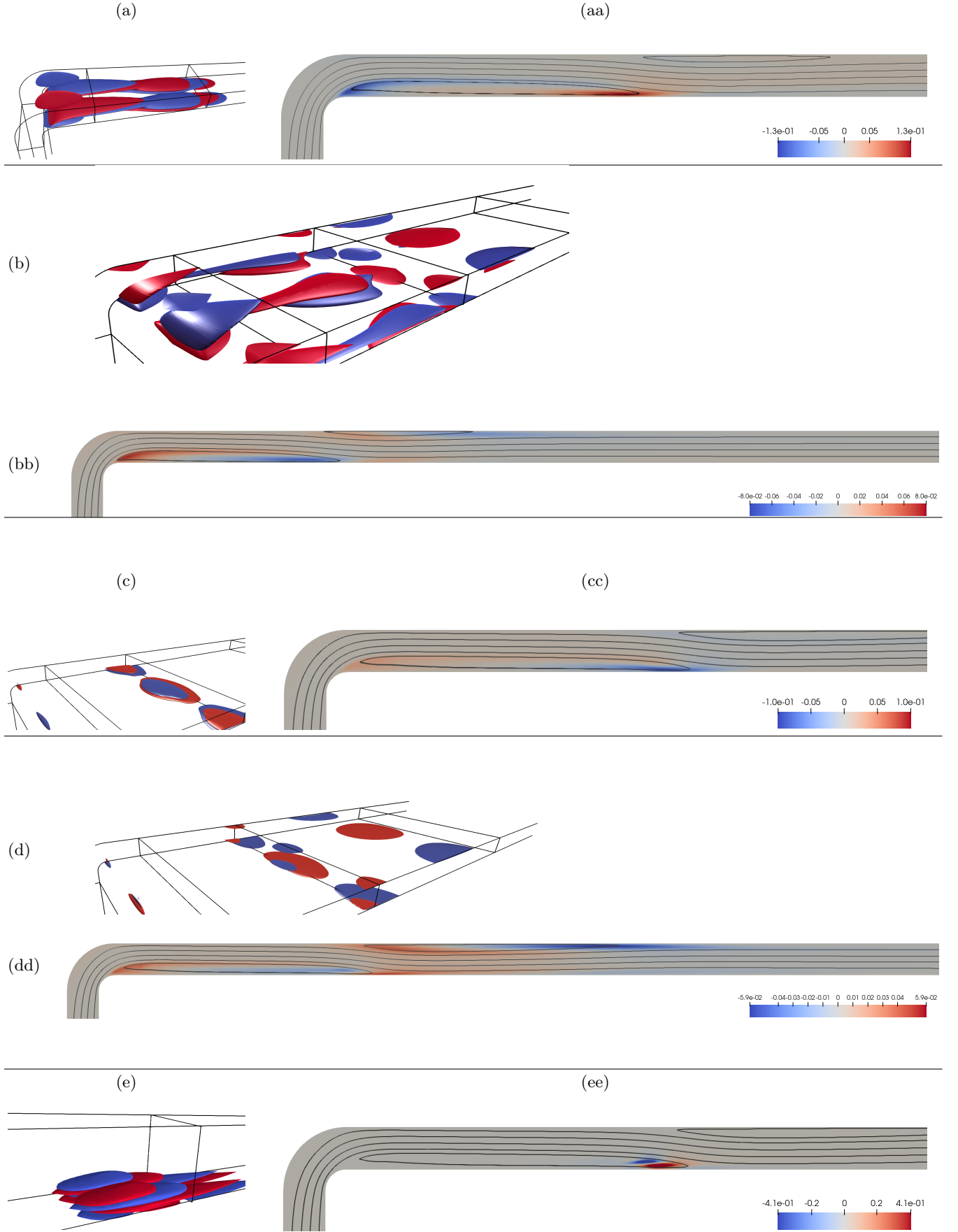


FIG. 14. The unstable modes visualisation: the bubble mode vorticity isosurfaces ± 0.1 (a, positive value is red, negative is blue) and v_z amplitude over the base flow streamlines, section at the maximal amplitude (aa) at $Re = 1100$, $\beta = 1$; the coupled mode vorticity isosurfaces ± 0.15 (b) and v_z amplitude over the base flow streamlines (bb) at $Re = 1000$, $k = 0.45$; the coupled complex mode vorticity isosurfaces ± 0.3 (real part of eigenfunction – c, complex part – d) and v_z amplitude over the base flow streamlines (real part – cc, complex part – dd) at $Re = 1600$, $\beta = 0.3$; the bubble tail mode vorticity isosurfaces ± 0.4 (a) and v_z amplitude over the base flow streamlines, section at the maximal amplitude (aa) at $Re = 1600$, $\beta = 3$

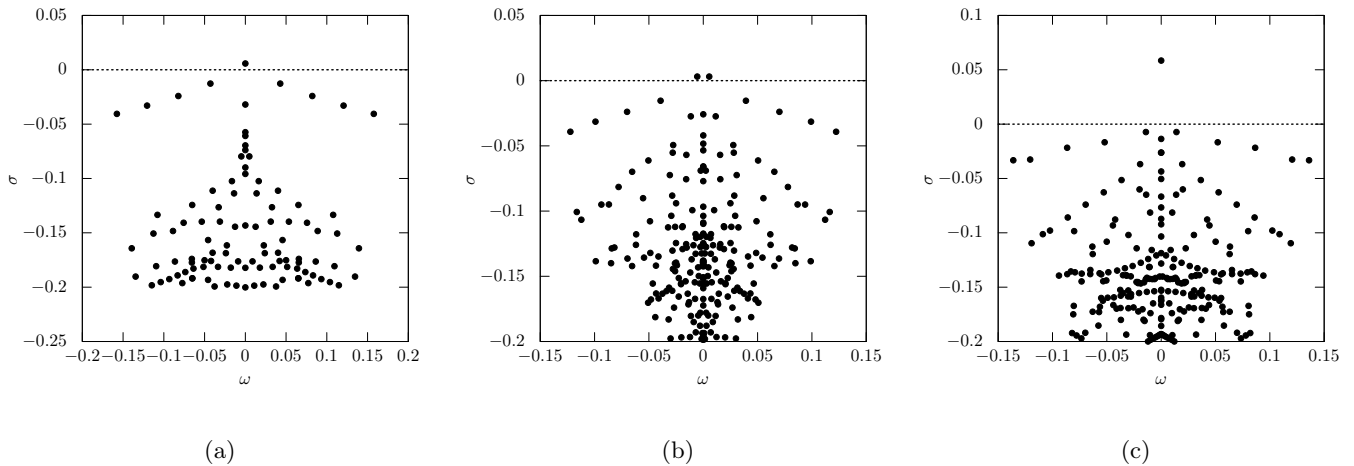


FIG. 15. The eigenvalues at $Re = 1100$, $\beta = 1$ (a); $Re = 1600$, $\beta = 0.3$ (b); $Re = 1600$, $\beta = 3.0$ (c)

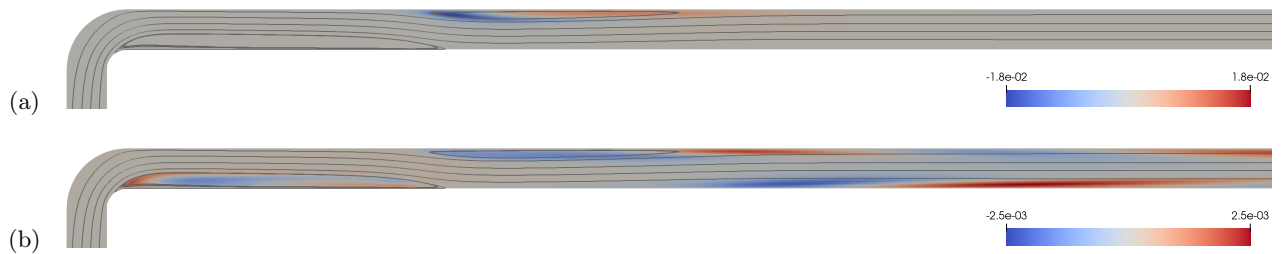


FIG. 16. v_z amplitude over the base flow streamlines for selected minor modes, section at the maximal amplitude. $Re = 1400$, $\beta = 1.0$ (a), $\beta = 0.4$ (b)

- degree sharp bend. *Journal of Fluid Mechanics*, 822:813–847, 2017.
- ¹⁰Gunnar Heskestad. Two-dimensional miter-bend flow. *Journal of basic engineering*, pages 433–443, 1971.
- ¹¹Hiroshi YAMASHITA, Ryotaro IZUMI, Genichiro KUSHIDA, and Takashi MIZUNO. Fluid flow and heat transfer in a two-dimensional miter-bend: 1st report, experiments and analyses. *Bulletin of JSME*, 29(258):4164–4169, 1986.
- ¹²Daichi Matsumoto, Koji Fukudome, and Hirofumi Wada. Two-dimensional fluid dynamics in a sharply bent channel: Laminar flow, separation bubble, and vortex dynamics. *Physics of Fluids*, 28(10):103602, 2016.
- ¹³Alan Charles Hurd and AR Peters. Analysis of flow separation in a confined two-dimensional channel. *Journal of basic engineering*, pages 908–914, 1970.
- ¹⁴P Orlandi and D Cunsolo. Two-dimensional laminar flow in elbows. *Journal of Fluids Engineering*, pages 276–283, 1979.
- ¹⁵NAE Kotb, MR Mokhtarzadeh-Dehghan, and AJ Ward-Smith. A numerical study of laminar and turbulent flows in a two-dimensional bend with or without a guide vane. *International journal for numerical methods in engineering*, 26(1):245–262, 1988.
- ¹⁶Donghun Park and Seung O Park. Streamwise streaks and secondary instability in a two-dimensional bent channel. *Theoretical and Computational Fluid Dynamics*, 28(3):267–293, 2014.
- ¹⁷L Niu and Hua-Shu Dou. Stability study of flow in a 90 bend based on the energy gradient theory. In *IOP Conference Series: Materials Science and Engineering*, volume 52, page 022006. IOP Publishing, 2013.
- ¹⁸Valerio Lupi, Jacopo Canton, and Philipp Schlatter. Global stability analysis of a 90-degree bend pipe flow. *International Journal of Heat and Fluid Flow*, 86:108742, 2020.
- ¹⁹George Em Karniadakis, Moshe Israeli, and Steven A Orszag. High-order splitting methods for the incompressible Navier-Stokes equations. *Journal of computational physics*, 97(2):414–443, 1991.
- ²⁰David Moxey, Chris D Cantwell, Yan Bao, Andrea Cassinelli, Giacomo Castiglioni, Sehun Chun, Emilia Juda, Ehsan Kazemi, Kilian Lackhove, Julian Marcon, et al. Nektar++: Enhancing the capability and application of high-fidelity spectral/hp element methods. *Computer Physics Communications*, 249:107110, 2020.
- ²¹Spencer J Sherwin and Mark Ainsworth. Unsteady navier-stokes solvers using hybrid spectral/hp element methods. *Applied Numerical Mathematics*, 33(1-4):357–363, 2000.
- ²²Espen Åkervik, Luca Brandt, Dan S Henningson, Jérôme Hoepffner, Olaf Marxen, and Philipp Schlatter. Steady solutions of the Navier-Stokes equations by selective frequency damping. *Physics of fluids*, 18(6):068102, 2006.
- ²³Bastien E Jordi, Colin J Cotter, and Spencer J Sherwin. An adaptive selective frequency damping method. *Physics of Fluids*, 27(9):094104, 2015.
- ²⁴Bastien E Jordi, Colin J Cotter, and Spencer J Sherwin. Encapsulated formulation of the selective frequency damping method. *Physics of Fluids*, 26(3):034101, 2014.
- ²⁵Alexander V Proskurin. Mathematical modelling of an unstable bent flow using the selective frequency damping method. *arXiv preprint arXiv:2011.02646*, 2020.

- ²⁶Alexander V Proskurin and Anatoly M Sagalakov. A numerical approach for transient magnetohydrodynamic flows. *arXiv preprint arXiv:1911.11909*, 2019.
- ²⁷Alexander V Proskurin and Anatoly M Sagalakov. The evolution of non-linear disturbances in magnetohydrodynamic flows. In *Journal of Physics: Conference Series*, volume 1, page 012062. IOP Publishing, 2019.
- ²⁸Edouard Boujo and François Gallaire. Sensitivity and open-loop control of stochastic response in a noise amplifier flow: the backward-facing step. *Journal of Fluid Mechanics*, 762:361–392, 2015.